DOI: 10.1002/chem.200800148

Aggregation Behavior and Dynamics of Synthetic Amphiphiles That Self-Assemble to Anion Transporters

Elizabeth K. Elliott,[c] Megan M. Daschbach,[c] and George W. Gokel*[a, b]

Abstract: The amphiphilic heptapeptides—referred to as synthetic anion transporters (SATs)—mediate chloride transport in planar lipid bilayer membranes, synthetic liposomes, and mammalian cells. The SATs described have the general formula $R^1{}_2NCOCH_2OCH_2CO$-$(Gly)_3$-Pro-$(Gly)_3$-OR^2. Substitution at R^1 and R^2 with various aliphatic or aromatic groups alters the ability of SATs to transport chloride through a phospholipid bilayer membrane. Despite extensive structure-activity relationship studies concerning Cl^--mediated transport by SATs, relatively little was known about the mechanism of insertion and pore-formation in the membrane. In the current study, the mechanistic behavior of SATs was investigated in aqueous solution and at the air–water interface. In the latter case, Langmuir trough studies and Brewster angle microscopy (BAM) revealed the extent of monolayer stability and organization for SATs. Dynamic light scattering and transmission electron microscopy (TEM) confirmed these results and defined the aggregation behavior of SATs in solution. SAT derivatives that showed low chloride transport activity organized into stable monolayers at the air–water interface, while more active SATs formed less stable monolayers. The relationship between intermolecular organization of SATs and pore-formation in the membrane is discussed along with its implications for chloride transport.

Keywords: aggregation · langmuir trough · membrane dynamics · self-assembly · synthetic ion channels

Introduction

During the past 20 years, an increasingly broad range of synthetic ionophores, pore-formers, and channel model compounds or assemblies has been designed, prepared, and their transport properties have been evaluated.[1] A considerable portion of this interest has focused recently on the development and characterization of synthetic anion transporters and channels.[1–6] Current, key challenges are to demonstrate the transport capabilities of a model channel system[7] and then to understand the structure and dynamics of the functioning transporter.[8,9] In this report, we bring to bear an array of analytical methods that have thus far been little used in this area.

We have developed a series of amphiphilic, heptapeptide-based channels known as synthetic anion transporters (SATs). Extensive structure–activity relationship studies have demonstrated that these molecules form selective chloride-conducting pores in liposomes[10] and planar bilayer membranes,[11] and they transport chloride ions in mammalian cells.[12] The general formula for amphiphilic SAT molecules in the current study is $R^1{}_2NCOCH_2OCH_2CO$-$(Gly)_3$-Pro-$(Gly)_3$-OR^2, where R^1 and R^2 are aliphatic or aromatic.

Varying the *N*- and *C*-terminal residues (R^1 or R^2, respectively) in these SAT molecules significantly affects transport efficacy.[13] The original SAT design featured two octadecyl chains at the *N*-terminus that were incorporated to aid in membrane insertion. When R^1 was shortened, channel activity increased, but anion selectivity decreased. A benzyl moiety was initially present at R^2 to prevent ionization of the *C*-terminal carboxyl group. Variations in R^2 (ethyl, isopropyl, *n*-heptyl, *n*-decyl, or *n*-octadecyl) revealed that *C*-terminal ester chains of intermediate length (*n*-heptyl, *n*-decyl) exhibited the highest chloride transport efficacy. These findings clearly revealed the efficacy of the transporters once they were present and functioning in the bilayer,

[a] Prof. Dr. G. W. Gokel
Departments of Chemistry & Biochemistry and Biology
Center for Nanoscience, University of Missouri–St. Louis
St. Louis, MO 63121 (USA)
E-mail: gokelg@umsl.edu

[b] Prof. Dr. G. W. Gokel
Department of Developmental Biology
Washington University, St. Louis, MO 63130 (USA)

[c] E. K. Elliott, M. M. Daschbach
Department of Chemistry
Washington University, St. Louis, MO 63130 (USA)
Fax: (+1) 314-516-5342

but it is equally important to understand how they aggregate in the bulk aqueous phase and/or insert into the membrane.

When SAT monomers form a pore, several discrete processes must occur.[14] The amphiphile is typically injected into the aqueous, liposome-containing suspension in an organic solvent. The solvent presumably disperses immediately, leaving a suspension of the amphiphiles in water. These amphiphiles may insert into the bilayer or aggregate in water into new assemblies. If the latter occurs, vesicular fusion may be required for the synthetic transporter to penetrate the membrane. In this case, self-assembly/deaggregation is a critical precursor step to pore-formation.

We report here an investigation of aggregation behavior using a Langmuir trough and Brewster angle microscopy (BAM) in conjunction with dynamic light scattering (DLS) and transmission electron microscopy (TEM). Both DLS and TEM give information on the aggregation behavior of SATs in the bulk aqueous phase, which has implications for membrane insertion dynamics. The air–water interface serves as a valuable model system for the membrane–aqueous interface of a cell. We address the questions of aggregation and molecular organization of the amphiphiles themselves, with an eye to correlating the behavior we observe with what is already known about the transport efficacy of SATs. To our knowledge, this is the first effort to explore these issues for a synthetic transporter system.

Results and Discussion

Compounds studied: Eleven different amino acid-containing amphiphiles were the subject of the present study; their syntheses have been previously reported (see Experimental Section for reference citations). They have the general form $R^1{}_2NCOCH_2OCH_2CO$-$(Gly)_3$-Pro-$(Gly)_3$-OR^2 in which R^1 and R^2 are varied. The residue R^1 is the hydrophobic, *N*-terminal anchor for the heptapeptide-based amphiphiles. These normal alkyl groups were varied from 6 to 18 in two-carbon increments. When R^1 was varied, R^2 was always benzyl. In the second group of structures, R^1 was always octadecyl ($R^1 = C_{18}H_{37}$) and R^2 was varied as follows: ethyl, isopropyl, *n*-heptyl, *n*-decyl, and *n*-octadecyl.

Transport efficacy of 1–11: Since the goal of this study was to understand how structural variations affected aggregation behavior and insertion dynamics, it was important to evaluate only compounds that are functional. The graphs of Figure 1 show chloride release data for compounds **1–11** in liposomes. Clearly, *N*- and *C*-terminal substituents have an effect on the SAT's ability to transport ions across a membrane. The *N*-terminal alkyl chains vary in length in compounds **1–6**. The chloride transport efficacy of **1–6** follows the trend **2** > **1** > **3** > **4** = **6** > **5**, where SATs with shorter *N*-terminal alkyl chains tend to have a higher chloride transport rate. In compounds **6–11**, the *C*-terminal ester group is either benzyl or alkyl and their relative transport activities are as follows: **9** > **10** > **6** = **11** > **7** > **8**.

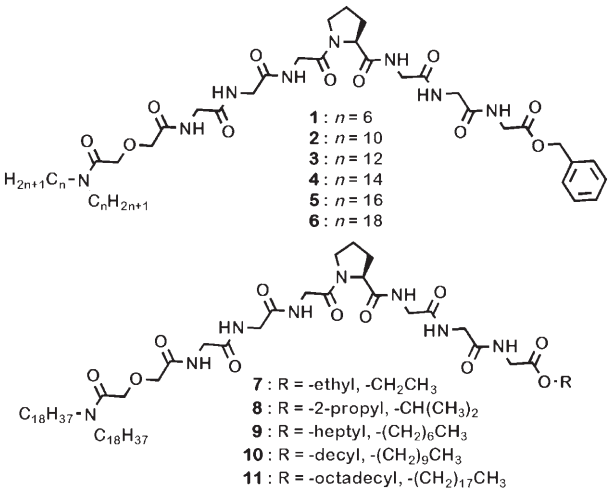

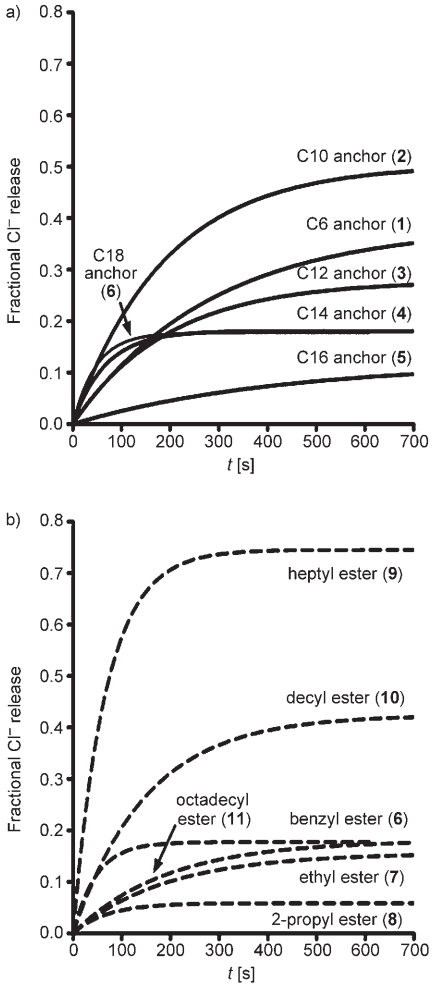

Figure 1. Relative chloride release from liposomes for compounds a) **1–6** and b) **6–11** as determined by ion-selective electrode. [Compound] = 65 μM, liposomes 7:3 DOPC/DOPA mixture, external buffer = 600 mM KCl, 10 mM HEPES, pH 7.0, internal buffer = 400 mM K_2SO_4, 10 mM HEPES, pH 7.0. [liposomes] = 0.31 mM (a, *N*-terminal variants), 0.20 mM (b, *C*-terminal variants).

Among **6–11**, the *C*-terminal esters of intermediate alkyl chain length (*n*-heptyl and *n*-decyl) have the highest chloride transport efficacy.

Langmuir trough studies of compounds 1–6: In the series **1–6**, the *N*-terminal hydrocarbon chains vary from hexyl to octadecyl in two-carbon increments. Surface pressure–area (π–A) isotherm data were obtained by using a Langmuir trough for **1** ($R^1=C_6H_{13}$), **2** ($R^1=C_{10}H_{21}$), **5** ($R^1=C_{16}H_{33}$), and **6** ($R^1=C_{18}H_{37}$). Three patterns of behavior are observed for these four compounds (see Figure 2). Compound **1** (*n*-hexyl, the shortest hydrocarbon) does not show typical monolayer behavior. Instead, the pressure gradually increased upon barrier compression and there were neither clear transition points nor was there evidence of collapse. When the hydrophobic chain (R^1) was *n*-decyl (**2**), the isotherm showed a single inflection point between the expanded and condensed phases. Monolayer collapse occurred at 65 $Å^2$ for compound **2** after reaching a surface pressure of 42 $mN\,m^{-1}$. Similar behavior was observed for **5** ($R^1=C_{16}H_{33}$). The isotherm data for compounds **3** (*n*-dodecyl) and **4** (*n*-tetradecyl), were similar to those observed for **2** and **5** and are not shown. All four of these compounds (**2–5**) reached a surface pressure of $\approx$45 $mN\,m^{-1}$ before collapse.

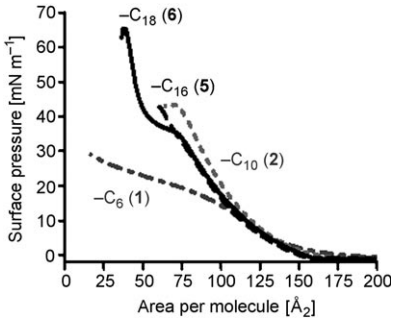

Figure 2. Surface pressure-area isotherm data for $(R)_2NCOCH_2OCH_2CO$-$(Gly)_3$-Pro-$(Gly)_3$-OCH_2Ph. R = C_6H_{13} (**1**), $C_{10}H_{21}$ (**2**), $C_{16}H_{33}$ (**5**), $C_{18}H_{37}$ (**6**).

Compound **6** has the longest hydrocarbon chain (*n*-octadecyl) in the series and forms the most stable monolayer. The isotherm of **6** showed three phase transitions before collapse, whereas no more than one transition was observed for the other compounds in the series. Compound **6** exists in the liquid-expanded phase between 161 and 74 $Å^2$ and enters the liquid-condensed phase at 52 $Å^2$. Among compounds **1–6**, *n*-octadecyl derivative **6** reached the highest surface pressure (65 $mN\,m^{-1}$) and the smallest molecular area (40 $Å^2$) prior to collapse. The 40 $Å^2$ minimum molecular area observed in the π–A isotherm of **6** corresponds to the known cross-sectional area occupied by the two alkyl chains, in this case *N*-terminal octadecyl chains.[15] From the number of transitions observed in the π–A isotherm of **6**, the large surface pressure, and small molecular area at monolayer collapse, we infer that **6** forms a highly organized monolayer.

In the series **1–6**, the compounds having the longest *N*-terminal hydrocarbon chains exhibited the greatest monolayer stability. This seems reasonable because the hydrocarbon chains align and longer chains should interact more strongly than short ones. Hexyl derivative **1** has the shortest hydrocarbon chains, and fails to form a stable monolayer. The closely related compounds **2–5** all form monolayers at the air–water interface, but each is less stable than that formed by **6**.

Determination of particle size in aqueous solution for compounds 1, 3, and 6: As noted above, **1–11** are all synthetic anion transporters. These molecules first insert into the liposomal bilayer, dimerize or oligomerize to form a functional pore, and chloride is subsequently released. These molecules are amphiphiles as well as ionophores so a possible "pre-aggregation" could occur before insertion into the liposomal bilayer. If so, the rate of pore formation and thence ion release would be directly affected.

In order to test for aggregate formation in aqueous solution, compounds **1** (R = hexyl), **3** (R = dodecyl), or **6** (R = octadecyl) were first dissolved in 2-propanol. An aliquot of each solution was added to 2 mL of Milli-Q water (pH $\approx$5.5) for a final concentration of 10 μM in aqueous solution. The suspensions were sonicated for 1 min. Dynamic light scattering (DLS) was used to determine the average effective diameter and the size distribution for the aggregates formed in each of these suspensions in pure water. Attempts were made to measure aggregation behavior in aqueous buffer (NaCl, $NaNO_3$, or KNO_3), but the formation of a precipitate prevented reproducible data collection.

At a starting concentration of 10 μM, a solution of compound **6** (R = octadecyl) formed spherical aggregates (see below) with an average effective diameter of 196 nm and a fairly narrow size distribution (Figure 3). These aggregates are similar in size to the phospholipid vesicles that were used in the Cl^- ion release studies described previously and above. In contrast, reproducible data could not be obtained for either **1** (hexyl) or **3** (dodecyl) at 10 μM, presumably because the aggregates were too small to detect or simply absent.

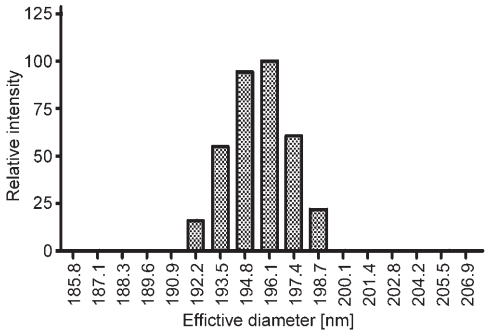

Figure 3. Typical size distribution as determined by dynamic light scattering (DLS) in solution for $(C_{18}H_{37})_2NCOCH_2OCH_2CO$-$(Gly)_3$-Pro-$(Gly)_3$-$OCH_2Ph$ (**6**).

Since no aggregation of **1** or **3** was observed at 10 μM, the concentration of compound **1** (R = hexyl) was increased in 10 μM increments from 10 to 100 μM. Even at a 10-fold higher concentration, reproducible data were not obtained. The concentration of compound **3** was also increased incrementally as done for **1**. When the concentration of **3** reached 60 μM, two populations of aggregates were observed centered near ≈30 and ≈200 nm. The bimodal distribution was reproducible; in no case was a single population observed. Similar behavior was observed when the concentration of **3** was 70 μM, but a precipitate formed at higher monomer concentrations. Typical data for **3**, showing the two populations, are apparent in the graph of Figure 4.

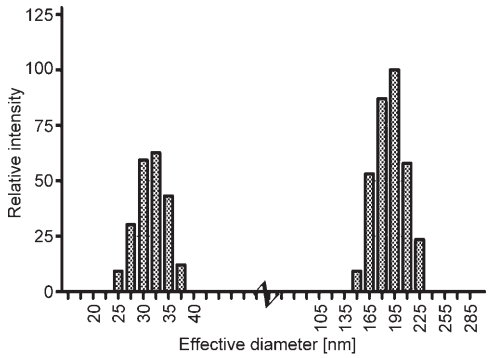

Figure 4. Typical size distribution as determined by dynamic light scattering (DLS) in solution for $(C_{12}H_{21})_2NCOCH_2OCH_2CO$-$(Gly)_3$-Pro-$(Gly)_3$-$OCH_2Ph$ (**3**).

Comparative behavior of 1–6: Dynamic light scattering showed that compounds **1** and **3** failed to aggregate in aqueous suspension at 10 μM while **6** reproducibly gave stable aggregates at this concentration. As noted above, studies using the Langmuir trough (Figure 2) showed that **6** formed a stable monolayer while **1**–**5** did not. In previous work, we found that **6** gave lower transport but higher selectivity than shorter-chained compounds.[16] We infer from the data obtained here that its octadecyl chains permit it to form a more stable and well-organized pore within the bilayer although the formation of such a pore may be impeded by self-aggregation. To the extent that the shorter-chained compounds do not aggregate, they may insert into the bilayer more rapidly, form pores more rapidly, and present a higher apparent transport efficacy.

TEM images of amphiphilic aggregates of 3 and 6: Figure 5 shows transmission electron micrographs of aggregates obtained from compounds **3** and **6**. Panel a) of Figure 5 shows an aggregate of **3** captured on a copper grid. It is approximately spherical and has a diameter of about 200 nm, as observed in dynamic light scattering experiments. This sample was prepared by dipping the copper grid into an aqueous suspension of **3** every 15 minutes during 2 h. We note that none of the TEM images required stain for visualization. Presumably, some monomer was also present in suspension

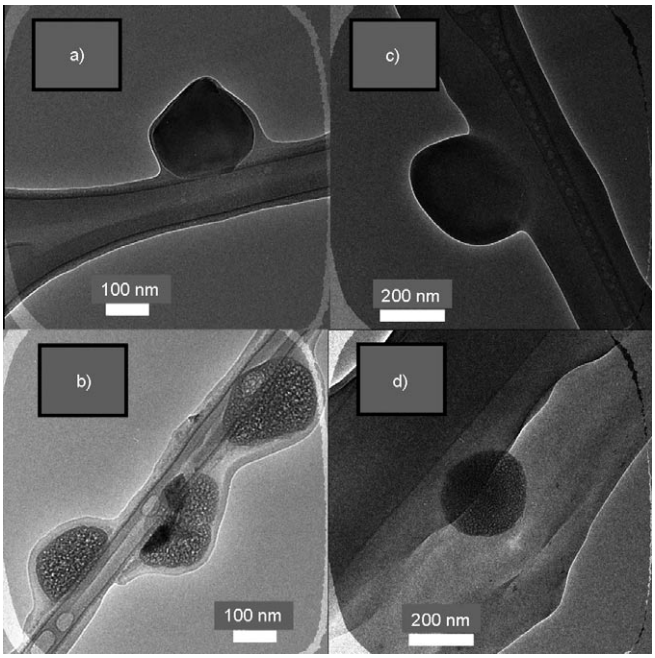

Figure 5. Transmission electron micrographs (TEM) of spherical aggregates comprised of monomers of compound **3**, $(C_{12}H_{25})_2NCOCH_2OCH_2CO$-$(Gly)_3$-Pro-$(Gly)_3$-$OCH_2Ph$ on a a) copper grid and b) carbon film. TEM of spherical aggregates formed from **6**, $(C_{18}H_{37})_2NCOCH_2OCH_2CO$-$(Gly)_3$-Pro-$(Gly)_3$-$OCH_2Ph$ on a copper grid c) and d). c) and d) are similar but d) shows fine structure.

and the formation of a thin membrane surrounding the vesicle and extending onto the grid is apparent in the micrograph. It is unknown whether this membrane is present in the aqueous suspension or is an artifact of the sample preparation process. Such phenomena are known when certain polymer samples are visualized by using this technique.[17] Panel b) of Figure 5 shows aggregates formed from **3**, as in panel (a), but visualized on a carbon film. Aggregate size is generally similar in the two samples and a membrane of the type noted in panel a) is also present here.

Panels c) and d) show nearly spherical aggregates of **6**, approximately 200 nm in size, that were visualized by TEM on a copper grid. The two panels represent two different experiments and confirm the reproducibility of this effort. Further, fine structure is apparent in the illustration of panel d) that is less apparent in c), owing to better focus in the former.

Dioctadecyl compound **6** forms ≈200 nm aggregates in aqueous suspension, as detected by DLS. These aggregates could be captured in electron micrographic images on copper grids and these sizes correlated well with the previous values. When **6** was spread at the air–water interface (Langmuir trough), a stable monolayer formed that could be characterized by an area at collapse of ≈40 Å. In contrast, didodecyl-chained **3** did not form stable aggregates in aqueous suspension (at 10 μM, DLS) nor did it form a stable monolayer in the Langmuir trough. The TEM images show smaller, less symmetrical aggregates than were formed by **6**. The smaller aggregates of **3** are not shown because they

were unstable in the electron beam. Additionally, aggregates of **3** could be obtained only at higher monomer concentrations than used for **6**.

Surface pressure–area (π–A) isotherm data for compounds 6–11: Synthetic anion transporter (SAT) monomers in the series **6–11** share the general formula $(C_{18}H_{37})_2NCOCH_2OCH_2CO$-$(Gly)_3$-Pro-$(Gly)_3$-$OR^2$. The *C*-terminal ester group is either aromatic (benzyl, **6**) or aliphatic (**7–11**). The alkyl groups in **7–11** are as follows: **7**, ethyl; **8**, isopropyl; **9**, *n*-heptyl; **10**, *n*-decyl; and **11**, *n*-octadecyl. Previous structure–activity relationship studies[14] showed that chloride transport changed dramatically with the identity of the *C*-terminal ester residue (see Figure 2). The most active esters were *n*-heptyl (**9**) and *n*-decyl (**10**), while the *n*-octadecyl ester was nearly inactive. The dependence of chloride transport on the structure of the *C*-terminal ester suggested that this residue serves as a secondary membrane anchor for the SAT molecule.

The Langmuir trough is ideal for the study of these amphiphilic elements. Thus, monolayers of compounds **6–11** were individually formed at the air–water interface and π–A isotherms were collected on a Langmuir trough. The isotherm data for **6–11** fall into two categories. Data for the most active compounds, **9** (*n*-heptyl) and **10** (*n*-decyl) are shown in Figure 7 and isotherms for the less active compounds are shown in Figure 6, below. The combined data are summarized in Table 1 (see below).

Table 1. Summary of transition points in surface pressure-area isotherms obtained by using a Langmuir trough.

	X in $(C_{18}H_{37})_2NCOCH_2OCH_2CO$-GGGPGGG-X	Phase transitions [Å^2]			
		1st	2nd	3rd	collapse
6	OCH_2Ph	161±2	74±1	52±1	40±1
7	OCH_2CH_3	156±8	70±4	55±3	41±2
8	$OCH(CH_3)_2$	179±8	76±4	57±2	42±3
9	OC_7H_{15}	176±6	n/a	n/a	68±4
10	$OC_{10}H_{21}$	167±4	n/a	n/a	70±2
11	$OC_{18}H_{37}$	147±2	74±1	n/a	57±1

The isotherm data shown in Figure 6 demonstrate that compounds **6**, **7**, **8**, and **11** form stable monolayers. The isotherm for each of these compounds shows two or three phase transitions and all exhibit high surface pressures ($>50\,mN\,m^{-1}$) at monolayer collapse. Isotherms for compounds **6**, **7**, and **8** share nearly identical transition points (the surface pressure for **6** is slightly higher). At ≈170 Å^2, monolayers of **6**, **7**, and **8** enter the liquid-expanded phase. Between 75–55 Å^2, monolayers of **6**, **7**, and **8** are in the liquid-expanded + liquid-condensed coexistence region. The high surface pressure of compound **6** (≈35 mN m^{-1}) between 74–52 Å^2 compared to **7** and **8** likely results from a high energy of solvation required for the *C*-terminal benzyl group in the aqueous subphase. From there, the monolayers enter the liquid-condensed phase before collapse at a surface pressure of 60 mN m^{-1}. The minimum molecular area observed for **6**, **7**, and **8** is about 40 Å^2 and represents the area occupied by the *N*-terminal dioctadecyl chains.[16]

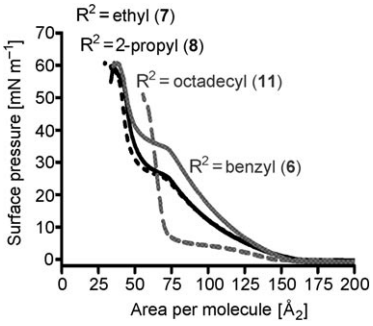

Figure 6. Surface pressure-area (π–A) isotherm data for $(C_{18}H_{37})_2NCOCH_2OCH_2CO$-$(Gly)_3$-Pro-$(Gly)_3$-$OR^2$. R^2 = benzyl (**6**), ethyl (**7**), isopropyl (**8**), and *n*-octadecyl (**11**).

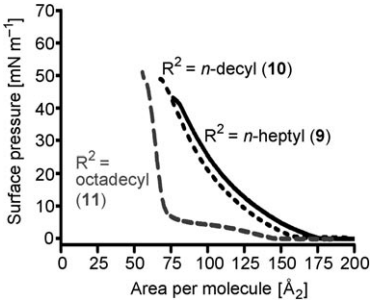

Figure 7. Surface pressure-area (π–A) isotherm data for $(C_{18}H_{37})_2NCOCH_2OCH_2CO$-$(Gly)_3$-Pro-$(Gly)_3$-$OR^2$. R^2 = *n*-heptyl (**9**), *n*-decyl (**10**) and *n*-octadecyl (**11**).

Compound **11** (R^2 = *n*-octadecyl) also forms a stable monolayer. Like the other compounds, it exhibits three phase transitions, two of which are well defined and the third is apparent from Brewster angle microscopy (see below). The first transition is apparent at 147 Å^2 at which point **11** enters the liquid-expanded phase. The horizontal portion of the isotherm between ≈115–75 Å^2 corresponds to the liquid-expanded + liquid-condensed coexistence phase for **11**. Compound **11** exists in the liquid-condensed phase between 74–57 Å^2 at which point monolayer collapse occurs. This molecular area (57 Å^2) is larger than observed for **6–8** (40 Å^2). The larger area is not surprising since **11** contains three octadecyl chains, compared to only two in **6–8**. These chains are presumably oriented at the air–water interface perpendicular to the aqueous phase and represent the minimum contact distance in each system. The ≈20 Å^2 difference in collapse areas between compounds **11** and **6–8** corresponds to the cross sectional area of this third octadecyl chain.

The areas at which collapse occurs (abscissa) is defined by the number of octadecyl chains in each molecule. The three octadecyl chains of **11** make it the most ordered of the monolayers. It is not the most stable monolayer among the four compounds, however, because the three hydrocarbon chains align only when the peptide's conformation is contorted to

permit it. A conformational reorganization of the peptide chain is not required to align the two adjacent (R^1) octadecyl chains of **6–8**, so the monolayer does not experience the peptide's conformational strain.

Differences in monolayer stability and organization were assessed by comparing the surface pressure values (ordinate) for each compound. The surface pressures apparent in the isotherm of compound **11** are distinct from those observed for **6–8** (Figure 6), which are similar to each other. The lower pressure experienced by **11** in the plateau region of the isotherm suggests that the monolayer is highly ordered (see the Brewster angle microscopy in Figure 8, below). However, the surface pressure at collapse ($60\,mN\,m^{-1}$) for compounds **6–8** suggests that **6–8** form more stable monolayers than does compound **11**. This situation is unusual because more ordered monolayers are typically also more stable. In the present case, monolayers of **6–8** are more stable while the monolayer of **11** is more ordered.

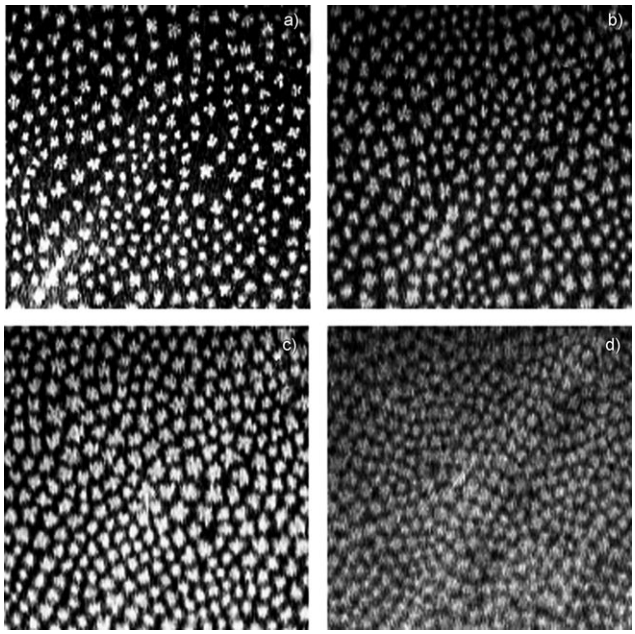

Figure 8. Brewster angle micrographs of **11** were captured at a) 114, b) 89, c) 81, d) 74 Å^2. Image field of view is 1.0 mm × 1.0 mm.

Figure 7 shows the π–A isotherms of compounds **9** and **10**, along with that for **11**. Compounds **9** and **10** were the most effective Cl^- transporters among the compounds in this study. The isotherm behavior for **9** and **10** is distinct from that observed for **6–8** and also from **11**, to which the *n*-heptyl and *n*-decyl chains seem more closely related. The isotherms for **9** and **10** each show a single transition before collapse occurs. It is clear that neither of these molecules forms a stable, highly organized monolayer. Compounds **9** and **10** enter the liquid-condensed phase near 170 Å^2 and reach a surface pressure of less than $50\,mN\,m^{-1}$ before collapse occurs at 70 Å^2. Monolayers of compounds **9** and **10** collapse at larger molecular areas and at lower surface pressures compared to monolayers of **6–8**, and **11**. The π–A isotherms show that monolayers of SAT compounds **9** and **10** are the least stable of the series **6–11**. The data for compounds **6–11** are summarized in Table 1.

Monolayer stability and chloride release: The π–A isotherms for compounds **6–11** suggest that **6**, **7**, **8**, and **11** form the most stable monolayers. The data of Figure 1 show that the most active transporters in this group are **9** and **10**, with **6–8** and **11** being poorer at releasing Cl^- from lipid vesicles. This approximately inverse relationship suggests that monomers that form less stable monolayers form more active chloride transporting pores within the bilayer.

There are two obvious explanations for this behavior. One is that the monomers that form more stable aggregates with each other interact more strongly with individual phospholipid monomers. This, in turn, means that their lateral diffusion through the membrane is slowed and the chance of finding a second monomer with which to form a pore is diminished. Alternately, the formation of stable aggregates in suspension could diminish the rate at which monomers insert into the phospholipid bilayer, reducing the kinetics of pore formation. Light scattering experiments in Milli-Q water suggested qualitatively that more stable (better organized, more reproducible) aggregates were formed from less active **6** and **11** (see also data below) than **9** (data not shown) and **3**. These observations favor the second of the two suggestions posed above.

Brewster angle microscopy of compound 11: An attempt was made to observe the organization of **6–11** by using Brewster angle microscopy (BAM). Distinct organization was observed only for **11**, which is in the cluster of least active pore-formers. Surface pressure-area (π–A) isotherm data showed that compound **11** forms a stable monolayer that undergoes several phase transitions (see above). We therefore visualized the organization by using BAM at the air-aqueous interface on the Langmuir trough. Selected images of the monolayer are shown in Figure 8.

Compound **11** forms ordered domains in the liquid-expanded + liquid-condensed coexistence region. These are apparent in panels a)–c). The dark regions of the monolayer contain the liquid-expanded phase while the bright snowflake-shaped domains are the liquid-condensed regions. Small, bright domains appear at areas of 140 Å^2. The increased compression is apparent in the increased proximity of aggregates from a)–d). In panel d), contrast is already diminished and the surface is nearly uniform. The uniform surface is featureless and is not shown. The diminished contrast at 74 Å^2 (panel d) corresponds to the transition (see Table 1 and Figures 6 and 7) to the liquid-condensed phase for compound **11**.

Dynamic light scattering and particle size analysis of 11: As noted above, none of compounds **1–11** formed stable aggregates in aqueous buffer, at least as judged by dynamic light

scattering. As described above, **3** and **6** form aggregates in Milli-Q water. Dynamic light scattering revealed a bimodal distribution for **11** (centered at ≈80 nm and a larger population centered at ≈275 nm, *see* Figure 9). Compared to **3** or **6**, aggregates of **11** were stable for days rather than hours. Owing to differences in monomer solubility, a variation in the experimental method was used to form the aggregates of **11** (see Experimental Section), but this should not affect aggregate stability.

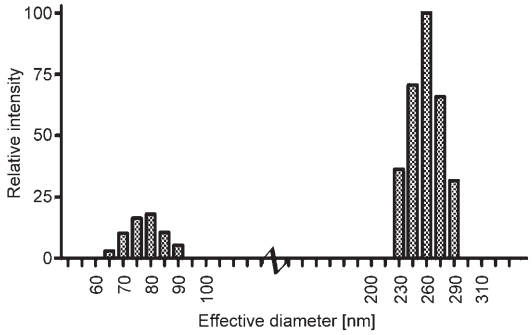

Figure 9. Typical size distribution as determined by dynamic light scattering for $(C_{18}H_{37})_2NCOCH_2OCH_2CO$-$(Gly)_3$-Pro-$(Gly)_3$-$OC_{18}H_{37}$ (**11**).

TEM images of 11: Transmission electron micrographs (TEM) were obtained for compound **11**. Figure 10 shows TEM images of the ≈275 nm spherical aggregates of **11**. The aggregates of **11** are not only more stable than those of **3** or **6**, but they are larger. The π–A isotherm data show that the molecular area of **11** at monolayer collapse is 57 Å^2, which corresponds to the close association of three alkyl chains. Figure 10 (panel a) shows a single spherical aggregate resting on the carbon-coated grid. It is nearly symmetrical and has a diameter of 275–285 nm. This agrees well with the particle size distribution obtained by light scattering in aqueous solution. Panel b) shows a cluster of similarly sized aggregates.

Relationship between monolayer formation and aggregation behavior: Compounds **6** and **11** are identical except for the *C*-terminal ester groups. Compound **6** is *C*-terminated by benzyl and **11** by *n*-octadecyl. Isotherms (π–A) of **6** and **11** both show three phase transitions but the collapse pressure for **6** is greater than for **11** indicating a higher ultimate stability of the condensed assembly (Figure 6). An important difference is that the π–A isotherms show that the minimum area for **6** is determined by the size of two alkyl chains while the minimum size of **11** corresponds to three alkyl chains. This means that the three alkyl chains of **11** are compressed and are likely in "cylindrical" contact but that the benzyl ester of **6** does not associate along its twin octadecyl chain's axis. Instead, it seems likely that the benzyl group of **6** is in contact with the aqueous subphase and stabilized by H-bond interactions with its π system. The longitudinal interaction of the three alkyl chains requires a greater compression of the heptapeptide chain, which makes **11** somewhat less stable overall than **6** (see Figure 11). The collapse pressures of 65 and 50 mN m^{-1} for **6** and **11**, respectively, clearly reflect this.

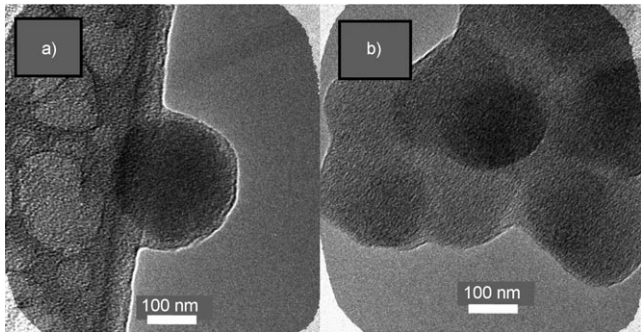

Figure 10. Transmission electron micrographs of aggregates of $(C_{18}H_{37})_2NCOCH_2OCH_2CO$-$(Gly)_3$-Pro-$(Gly)_3$-$OC_{18}H_{37}$ (**11**). a) Single ordered aggregate and b) cluster of ordered aggregates, bars represent 100 nm.

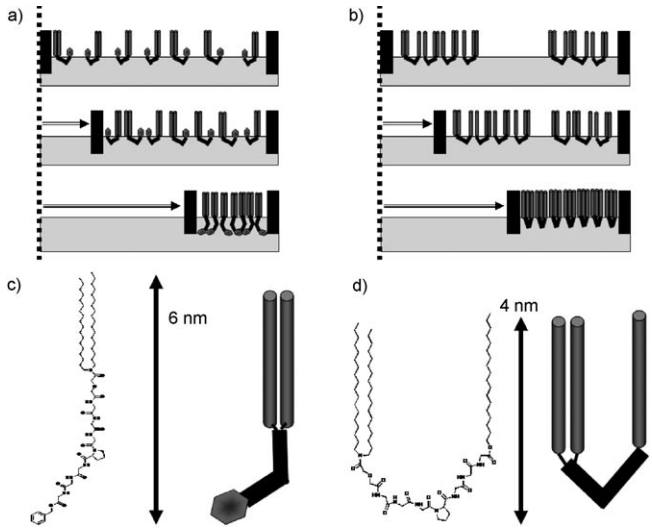

Figure 11. Proposed mechanism of monolayer formation of a) **6** and b) **11**. Approximate lengths for possible conformations of c) **6** and d) **11**.

It is interesting to note that although **6** formed a more stable monolayer than **11**, the latter is more organized. This unusual situation is supported by BAM images, which reveal that compound **11** forms ordered domains at a large molecular area, reflecting high intermolecular organization. The inability of the *C*-terminal octadecyl chain of **11** to be solvated in the aqueous subphase greatly restricts the number of conformations the heptapeptide sequence can assume. The *C*-terminal benzyl moiety in **6** is solvated in the subphase, which allows a wider range of motion of the heptapeptide.

Panels c) and d) of Figure 11 show schematically the results of CPK model building experiments. Based on the

measurements of CPK models of **6** and **11**, we estimate that a micelle of compound **6** would have a diameter of 12 nm and a micelle of **11** would have a diameter of 8 nm. Micelle formation is unlikely because DLS shows that **6** and **11** form larger aggregates than this in solution. These aggregates are stable for at least hours. The high reproducibility and narrow size distribution in the DLS experiments comport with TEM images of **6** and **11** which show that the aggregates are both spherical and symmetrical.

Conclusion

We have examined, using an array of analytical techniques, the amphiphilic behavior of a family of known synthetic anion transporters. We have assessed their ability to transport Cl^-, their ability to aggregate in an aqueous environment, and their monolayer stability at the air–water interface. We found that in general, as the *N*-terminal dialkyl chain length increased, so did the stability of the monolayer. The most stable monolayer was produced by **6**, which possesses twin octadecyl chains at the *N*-terminus. Compound **6** also produced the most stable and symmetrical aggregates in aqueous solution of the series **1**–**6**.

Substitution at the *C*-terminal ester position of SATs also affected monolayer stability, organization at the air–water interface, and aggregation behavior. Compounds **6** (benzyl) and **11** (octadecyl), which differ only at the *C*-terminus were remarkable because **6** gave a more stable monolayer than **11** but **11** was more organized than **6**. Langmuir trough and BAM studies clearly show this and correlate well with data obtained by DLS and TEM. Amphiphile monomers that form stable monolayers at the air–water interface also form spherical aggregates in solution. We therefore conclude that a higher level of molecular organization and stability in the amphiphilic monomers is deleterious to insertion in a phospholipid bilayer and formation of a functioning pore therein.

Experimental Section

Compound synthesis

$(C_6H_{13})_2$N-$COCH_2OCH_2CO$-$(Gly)_3$-Pro-$(Gly)_3$-OCH_2Ph (1) was prepared as previously reported.[14]

$(C_{10}H_{21})_2$N-$COCH_2OCH_2CO$-$(Gly)_3$-Pro-$(Gly)_3$-OCH_2Ph (2) was prepared as previously reported.[18]

$(C_{12}H_{25})_2$N-$COCH_2OCH_2CO$-$(Gly)_3$-Pro-$(Gly)_3$-OCH_2Ph (3) was prepared as previously reported.[14]

$(C_{14}H_{29})_2$N-$COCH_2OCH_2CO$-$(Gly)_3$-Pro-$(Gly)_3$-OCH_2Ph (4) was prepared as previously reported.[14]

$(C_{16}H_{33})_2$N-$COCH_2OCH_2CO$-$(Gly)_3$-Pro-$(Gly)_3$-OCH_2Ph (5) was prepared as previously reported.[14]

$(C_{18}H_{37})_2$N-$COCH_2OCH_2CO$-$(Gly)_3$-Pro-$(Gly)_3$-OCH_2Ph (6) was prepared as previously reported.[19]

$(C_{18}H_{37})_2$N-$COCH_2OCH_2CO$-$(Gly)_3$-Pro-$(Gly)_3$-OCH_2CH_3 (7) was prepared as previously reported.[14]

$(C_{18}H_{37})_2$N-$COCH_2OCH_2CO$-$(Gly)_3$-Pro-$(Gly)_3$-$OCH(CH_3)_2$ (8) was prepared as previously reported.[14]

$(C_{18}H_{37})_2$N-$COCH_2OCH_2CO$-$(Gly)_3$-Pro-$(Gly)_3$-$O(CH_2)_6CH_3$ (9) was prepared as previously reported.[14]

$(C_{18}H_{37})_2$N-$COCH_2OCH_2CO$-$(Gly)_3$-Pro-$(Gly)_3$-$O(CH_2)_9CH_3$ (10) was prepared as previously reported.[14]

$(C_{18}H_{37})_2$N-$COCH_2OCH_2CO$-$(Gly)_3$-Pro-$(Gly)_3$-$O(CH_2)_{17}CH_3$ (11) was prepared as previously reported.[14]

Monolayer studies: HPLC grade chloroform from Aldrich (St. Louis, MO) was used to prepare amphiphile solutions with a concentration of $\approx 1\,mg\,mL^{-1}$ as determined by mass. Surface pressure-area isotherm experiments were carried out on a Langmuir trough (Nima, UK). Pressure was measured with a Wilhelmy plate made out of filter paper. Subphase temperature was maintained at $23.0 \pm 0.1\,°C$ by an Isotemp 3016 circulating thermostat. The subphase contained ultrapure water with a resistivity of 18.2 MΩ (Millipore). Monolayers were formed by spreading 50 μL of a $CHCl_3$ solution of compounds **1**–**11** ($1.0\,mg\,mL^{-1}$) onto the subphase and allowing 10 minutes for the solvent to evaporate. Trough barriers were compressed at a constant speed of $< 0.3\,nm^2\,mlc^{-1}\,min^{-1}$. Data are plotted as surface pressure ($mN\,m^{-1}$) vs molecular area ($Å^2$). Isotherm data were collected in triplicate on each of 4 separate days, resulting in a total of 12 individual trials for each compound to obtain accurate isotherm information.

Dynamic light scattering: For compounds **1**, **3** and **6**, approximately 1 mg was dissolved in 1 mL HPLC grade hot 2-propanol in order to prepare 1 mM stock solutions. Between 20–200 μL was added to 2 mL ultrapure water (Millipore) in a Fisherbrand borosilicate disposable culture tube (16×100 mm). The culture tube and solution was sonicated in a Branson 1510 sonicator, at room temperature, for exactly 1 minute. For compound **11**, 11.76 mg (8.8 μmol) was dissolved in hot hexanes in a Fisherbrand borosilicate disposable culture tube (16×100 mm) and sonicated for exactly 2 minutes. To this was added 2 mL ultrapure (Millipore) water and 250 μL methanol. The entire contents of the culture tube were then transferred to a round bottom flask and the hexanes and methanol were slowly removed under reduced pressure (500 mbar, 35 °C) over a period of 5 h.

All aqueous solutions were then carefully transferred via pipette to a BI-SCP square, polystyrene cuvette, 10 mm in length, 4.5 mL in volume, from Brookhaven instruments. Dynamic light scattering measurements were performed on a 90Plus/BI-MAS multi angle particle sizing instrument from Brookhaven instruments. Data were collected at $25\,°C \pm 0.03$. The light source was a 15 mW solid state laser. Scattered light from the samples was collected at 90° from the incident light. Each trial consisted of 4 runs lasting 3 minutes per run, on thin shells mode, with a dust cutoff of 200. Each sample was measured 3 times on at least two different days, and the effective diameters are an average of at least six trials. Particle size distributions as determined by intensity were also recorded.

Transmission electron microscopy (TEM): TEM was performed on a JEOL JEM 2000 FX electron microscope operating at 200 kV. A GATAN CCD camera was used to digitize the images. To prepare the TEM sample of **6**, 1.17 mg (1.0 μmol) was dissolved in 1002 μL of hot HPLC grade 2-propanol. 20 μL of this solution was added to 2.00 mL of ultrapure water (Millipore) in a borosilicate culture tube resulting in a 10 μM solution. This solution was then sonicated for exactly 1 minute. To prepare the TEM sample of **3**, 0.58 mg (0.58 μmol) was dissolved in 580 μL of hot HPLC grade 2-propanol. 120 μL of this solution was added to 2.00 mL of ultrapure water (Millipore) in a borosilicate culture tube resulting in a 60 μM solution. This solution was then sonicated for exactly one minute. To prepare the TEM sample of **11**, 11.76 mg (8.84 μmol) was dissolved in 2.00 mL of hot HPLC grade hexanes. This solution was then sonicated for exactly 2 minutes. Immediately following sonication, 2.00 mL of ultrapure water (Millipore) in a borosilicate culture tube was added, followed by 250 μL of HPLC grade methanol. This was then transferred to a 25 mL round bottom flask, and the organic solvents were evaporated under reduced pressure (500 mbar, 35 °C) for 5 h. The residual aqueous layer was carefully transferred via pipette to another culture tube.

For the images collected on carbon grids, a copper grid coated with lacey carbon on formvar, 300 mesh (Ted Pella Inc.), was dipped into the solution and the water was allowed to evaporate. Because the solution was dilute, this process was repeated every 20 minutes for 2 h. After the dipping process was complete and the carbon film was completely dry, the film was placed on a single tilt sample holder and the images were collected.

For the image collected on a carbon film, an amorphous PELCO support film of formvar stabilized by carbon, 5–10 nm in thickness (Ted Pella, Inc.), was dipped once into the 60 μM solution of **3** and allowed to dry. This film was then placed directly onto a single tilt sample holder and the image was collected.

Brewster angle microscopy (BAM): BAM images were collected using a MicroBAM2 (Nanofilm Technology, Göttingen, Germany) fitted over the Langmuir trough. The light source is a 659 nm laser diode with 30 mW maximum optical power. The images were captured by a CCD camera and stored on a PC. Field of view for raw image is approximately 3.6 mm wide × 4.1 mm high. Images were adjusted using GIMP software to show a field of view of 1.0 mm × 1.0 mm in Figure 8. Barrier compression speed was 5 $Å^2$ $molecule^{-1}$ min^{-1}.

Acknowledgement

We thank the NIH (GM-36262, GM-63190) and NSF (CHE-0415586) for grants that supported this work.

[1] a) B. A. McNally, W. M. Leevy, B. D. Smith, *Supramol. Chem.* **2007**, *19*, 29–37; b) S. Matile, N. Sakai, *Anal. Meth. Supramol. Chem.* **2007**, 391–418; c) T. M. Fyles, *Chem. Soc. Rev.* **2007**, *36*, 335–347; d) R. S. Hector, M. S. Gin, *Supramol. Chem.* **2005**, *17*, 129–134.

[2] P. H. Schlesinger, R. Ferdani, J. Liu, J. Pajewska, R. Pajewski, M. Saito, H. Shabany, G. W. Gokel, *J. Am. Chem. Soc.* **2002**, *124*, 1848–1849.

[3] G. A. Cook, O. Prakash, K. Zhang, L. P. Shank, W. A. Takeguchi, A. Robbins, Y. X. Gong, T. Iwamoto, B. D. Schultz, J. M. Tomich, *Biophys. J.* **2004**, *86*, 1424–1435.

[4] N. Madhavan, E. C. Robert, M. S. Gin, *Angew. Chem.* **2005**, *117*, 7756–7759; *Angew. Chem. Int. Ed.* **2005**, *44*, 7584–7587.

[5] J. M. Mahoney, G. U. Nawaratna, A. M. Beatty, P. J. Duggan, B. D. Smith, *Inorg. Chem.* **2004**, *43*, 5902–5907.

[6] a) P. V. Santacroce, O. A. Okunola, P. Y. Zavalij, J. T. Davis, *Chem. Commun.* **2006**, 3246–3248; b) P. V. Santacroce, J. T. Davis, M. E. Light, P. A. Gale, J. C. Iglesias-Sanchez, P. Prados, R. Quesada, *J. Am. Chem. Soc.* **2007**, *129*, 1886–1887.

[7] R. I. Diaz, J. Regourd, P. V. Santacroce, J. T. Davis, D. L. Jakeman, A. Thompson, *Chem. Commun.* **2007**, 2701–2703.

[8] V. Gorteau, G. Bollot, J. Mareda, A. Perez-Velasco, S. Matile, *J. Am. Chem. Soc.* **2006**, *128*, 14788–14789.

[9] Y. Baudry, D. Pasini, M. Nishihara, N. Sakai, S. Matile, *Chem. Commun.* **2005**, 4798–4800.

[10] T. M. Fyles, *Curr. Opin. Chem. Biol.* **1997**, *1*, 497–505.

[11] P. H. Schlesinger, R. Ferdani, R. Pajewski, J. Pajewska, G. W. Gokel, *Chem. Commun.* **2002**, 840–841.

[12] R. Ferdani, G. W. Gokel, *Org. Biomol. Chem.* **2006**, *4*, 3746–3750.

[13] R. Pajewski, R. Garcia-Medina, S. L. Brody, W. M. Leevy, P. H. Schlesinger, G. W. Gokel, *Chem. Commun.* **2006**, 329–331.

[14] N. Djedovic, R. Ferdani, E. Harder, J. Pajewska, R. Pajewski, M. E. Weber, P. H. Schlesinger, G. W. Gokel, *New J. Chem.* **2005**, *29*, 291–305.

[15] H. W. Huang, *Biochim. Biophys. Acta Biomembr.* **2006**, *1758*, 1292–1302.

[16] A. E. Alexander, *Proc. Roy. Soc. London. Series A Math. Phys. Sci.* **1942**, *179*, 470–485.

[17] P. H. Schlesinger, N. K. Djedovic, R. Ferdani, J. Pajewska, R. Pajewski, G. W. Gokel, *Chem. Commun.* **2003**, 308–309.

[18] P. Li, J. M. Zhu, P. Sunintaboon, F. W. Harris, *Langmuir* **2002**, *18*, 8641–8646.

[19] P. H. Schlesinger, R. Ferdani, J. Pajewska, R. Pajewski, G. W. Gokel, *New J. Chem.* **2003**, *27*, 60–67.

Received: January 24, 2008
Published online: May 15, 2008

